CrossMark

TECHNICAL ARTICLE

Effect of Welding Processes on Microstructure, Mechanical Properties, and Corrosion Behavior of Low-Nickel Austenitic Stainless Steels

Ankur V. Bansod[1] · Awanikumar P. Patil[1]

Abstract In the present study, the influence of welding process on metallurgical, mechanical, and corrosion behavior of shielded metal arc welding and tungsten inert gas welding was explored using 308L electrode. Tungsten inert gas welding exhibited equiaxed grains, having better hardness and tensile strength than that of its counterpart. It is observed that heat-affected zone and unmixed zone of shielded metal arc welding is wider than tungsten inert gas welding. Dendrite length and inter-dendritic distance are smaller for tungsten inert gas welding. The volume fraction of ferrite is found to be higher in tungsten inert gas welding. The base metal shows higher ductility than both the weld; also, the ductility of tungsten inert gas welding was marginally better than shielded metal arc welding. Modified Strauss test shows intense grain dropping and strength reduction in both the process. The pitting corrosion resistance is found to be better for tungsten inert gas welding as compared to shielded metal arc welding. The galvanic current shows higher current density when couples are formed with base metal and weld zone produced by tungsten inert gas welding.

Keywords Shielded metal arc welding (SMAW) · Tungsten inert gas welding (TIG) · Modified Strauss test · Pitting corrosion · Galvanic corrosion

✉ Ankur V. Bansod
ankur.1754@gmail.com

Awanikumar P. Patil
appatil14@gmail.com

[1] Department of Metallurgical and Materials Engineering, Visvesvaraya National Institute of Technology (VNIT), Nagpur 440010, India

Introduction

Excellent weldability, formability, and corrosion behavior of classical austenitic steels (ASS's) are highly accepted grades in power sector, textiles, paper, and chemical industry. The development of ASS with improvement was started in 1960s and become a workhorse steel since the 1980s [1]. Nickel (Ni) content in ASS has stabilized the austenitic phase at room temperature. Ni is the prime austenitic stabilizer and costly alloying element, breaching the backbone of austenitic producer and end users. In the recent years, development of low Ni or Cr–Mn SS had attracted a great attention among the engineers and metallurgist. Cr–Mn SS is easily available and more economical than its predecessor [2, 3]. Cr–Mn SS also possesses higher strength and ductility as compared to 300 series stainless steels because of more effective solid-solution strengthening and also strong austenite stability, which reduces the tendency to form ferrite and deformation-induced α' and ε martensite [4, 5]. Therefore, high-potential low-nickel austenitic stainless steels can be utilized in industrial applications which include the shipbuilding industry, cryogenic processes, power-generating industry, railways, chemical equipment, nuclear industry, pressure vessels, and petroleum industry.

In fabrication, joining of metals is the most important process for any fabricated component. For joining of metals, fusion welding is widely used. There are various fusion welding processes like arc welding, resistance welding, electron beam welding, and laser beam welding. In arc welding, shielded metal arc welding (SMAW) and tungsten inert gas welding (TIG) are commonly used welding process in most of the industries, due to economical and portability. The main drawback of using SMAW and TIG welding process is the inability to weld

thick materials in a single pass. Tseng et al. [6] reported that 3-mm steel sheet can be easily welded by arc welding process in single pass. There are various parameters which had a strong influence on mechanical, metallurgical, and corrosion behavior of the material. Those parameters include heat input, selection of weld filler, welding processes, etc. Due to heterogeneity in welding from weld zone, heat-affected zone (HAZ) and base metal (BM) can lead to failure of metals in different environment conditions. As austenitic stainless steel (SS) are used in engineering applications, proper selection of filler and welding processes are highly important to get desired welding properties. Mohandas et al. [7] reported a comparative study of TIG and SMAW welding on 430 ferritic stainless steel and found greater strength and ductility in TIG welding as compared to SMAW. Galvis and Hormaza [8] worked on the characterization of failure modes for different welding processes of 304 SS and reported that SMAW, gas metal arc welding (GMAW), and flux core arc welding (FCAW) has minimum influence on the mechanical properties except mean grain size in the heat-affected zone (HAZ). Yayla et al. [9] reported that SMAW welding provides better toughness at the HAZ as compared to GMAW. Srinivasan et al. [10] investigated the microstructural and corrosion behavior using two different filler (duplex and austenitic filler) welded by SMAW welding process and concluded that general corrosion was better in weld metal welded by austenitic based filler. Kotecki et al. [11] has given WRC 1992 (welding research council) diagram to predict the solidification mode and the amount of ferrite content in weld. It is reported that small amount of ferrite in the weld zone is helpful in eliminating hot cracking [12]. Korino et al. [13] had found the recommended Cr–Ni equivalent ratio for ASS to be in between 1.52 and 1.9. The increase in the Cr–Ni equivalent ratio increases the strength in the weld. The reduction in δ ferrite in the weld metal by laser–TIG hybrid welding does not deteriorate the mechanical property of 304 ASS [14]. Srinivasan et al. studied the effect of heat input on fume generation and joint properties of gas metal arc-welded austenitic stainless steel and found that increase in heat input changes the microstructure of ferrite from vermicular ferrite to acicular and, further increase in heat input, to lathy ferrite. Also, the corrosion behavior depends upon the formation of ferrite [15]. Monte et al. performed the investigation on the grain size of HAZ by simulation and found to be 2 μm and further increasing the variable increases the width between 120 and 150 μm [16]. Raffi et al. [17] investigate on the microstructure and pitting corrosion of shielded metal arc-welded high-nitrogen stainless steel and found that the reduction in ferrite helps in improving the corrosion resistance. However, Subodh and Shahi [18] reported that the increase in delta ferrite in

GTAW welding process improves pitting resistance also, and the dendrite length and inter-dendritic distance decrease in increasing the heat input. Dadfar et al. [19] reported that the weld metal acts as cathodic part in the weldment and found a the reduction in corrosion rate of weld metal in 0.9 wt.% NaCl solution. From the literature reviewed on welding process, the welding process is extremely important for any fabrication industry to sustain more life of the component also it is observed that there are literature for 300 series SS [8, 12–14, 18]. However, there is no systematic investigation for Cr–Mn SS in correlating microstructural, mechanicalm and corrosion behavior for SMAW and TIG welding processes. Hence, in this present work, author attempts to comparatively study economical welding process and tried to investigate metallurgical, mechanicalm and corrosion behavior of welding of Cr–Mn SS.

Materials and Method

The Cr–Mn SS is used in this investigation as a rolled sheet having dimensions 75 mm × 100 mm with 3 mm thickness. The sheets were solution annealed at temperature of 1050 °C for 1 h followed by water quenching. The reason for solution annealing is to homogenize the material. The chemical compositions of the base metal (BM) and fillers are listed in Table 1. Butt welding was performed at a constant current of 100 A with 3.15-mm-diameter electrode for both the welding process. Above 100 A melting of the base metal was observed, and below 3.15-mm-diameter electrode, lack of penetration was observed. Hence, the current range is set 100 A with 3.15-mm-diameter electrode. Back plating is used for all the welding process. As the thickness of the sheet is less, and hence back plate is used to support adequate weld metal. The argon flow rate for TIG welding was 10 L/min. Schematic welding diagram is shown in Fig. 1. The input heats were calculated according to Eq 1.

$$\text{Heat input (HI) in kJ/mm} = V \times I/1000 \times S \qquad (1)$$

where V is the voltage, I is the current (A), and S is the welding speed (mm/s). The welding speed was measured manually known length of the plate (100 mm). Table 2 shows welding parameters used for different welding procedures. For microstructures, the samples were abraded on a series of emery papers (220, 320, 400, 600, 800, 1000, 1200 grit) followed by mirror polish (cloth polish using 0.75 μ alumina). The samples were then etched with Marble's reagent (10 g $CuSO_4$, 10 ml HCl and 10 ml water) for 3 s followed by washing and drying. Different weld regions were analyzed using optical and scanning electron microscope (SEM) attached with energy dispersive spectroscopy

Table 1 Chemical composition of steels in wt (%)

Elements	Cr	Mn	Si	Ni	P	S	C	N	Fe
Cr–Mn ASS	16.46	9.14	0.46	0.19	0.014	0.0104	0.13	0.06	Balance
SMAW electrode (308L-16)	20.00	1.7	0.8	10.0	0.01	0.02	0.01	–	Balance
TIG electrode (308 L)	20.30	1.5	0.7	10.2	0.01	0.02	0.01	–	Balance
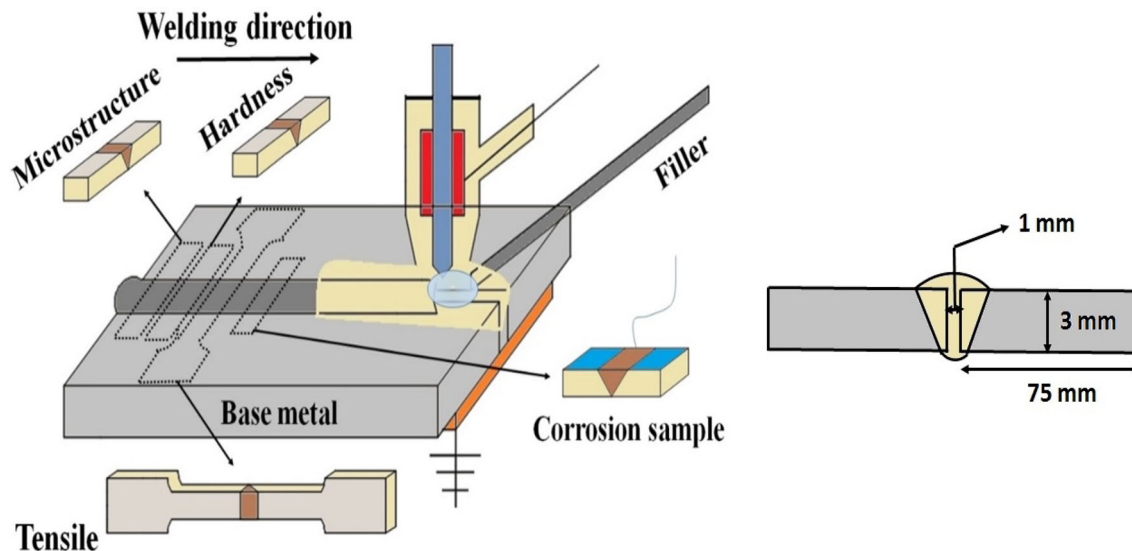
Fig. 1 Schematic diagram of welding

Table 2 Welding process parameters

Process	Welding current (I)	Welding voltage (V)	Speed (mm/s)	Heat input (kJ/mm)
SMAW	100	24	1.47	1.63
TIG welding	100	22	1.55	1.41

(EDS). Microhardness is measured along the transverse direction with the load of 0.5 kg with 15 s dwell time. Tensile test were carried out using universal testing machine as per ASTM E8 M-04 standard. Fracture test was analyzed using SEM. The ferrite content in the BM and weld zone was measured using ferritoscope. The result of ferritoscope measured is reported by ferrite number (FN). The potentiodynamic polarization tests were performed using potentiostat in 3.5% NaCl solution at room temperature (30 ± 1°C). Three-electrode electrochemical cells were used with platinum as a counter electrode, saturated calomel electrode (SCE) as the reference electrode, and test sample (10 mm × 10 mm) as working electrode. Potentiostatic cleaning was carried out at the beginning of the test to remove pre-formed film from the surface. All the test solution were purged (with nitrogen gas) for 1 h. The potentiodynamic polarization test is carried out at the scan rate of 0.1667 mV/s and potential range from −0.4 V SCE (vs OCP) to 0 V SCE (vs Ref) for evaluating the electrochemical corrosion behavior. The Tafel slope is used for generating electrochemical polarization data. Modified

Strauss test was performed, and in this test the tensile sample was boiled for 24 h in $CuSO_4$–H_2SO_4 solution, and the fracture surface was analyzed using SEM. Galvanic corrosion were performed using zero resistance ammeter for 3 h in 3.5% NaCl solution.

Result and Discussion

Microstructure

Figure 2a and b shows optical micrograph of base metal (as-received and solution annealing). It is found that base metal shows austenitic structure with twinning. WRC-1992 diagram is used for prediction of solidification mode and the amount of ferrite present in SMAW and TIG weld metals as shown in Fig. 3 using Eqs 2 and 3 [11].

$$Cr_{eq} = Cr + Mo + 0.7\ Nb \tag{2}$$

$$Ni_{eq} = Ni + 35C + 20N + 0.25Cu \tag{3}$$

Fig. 2 Optical microscope of base metal (**a**) as received (**b**) solution annealing
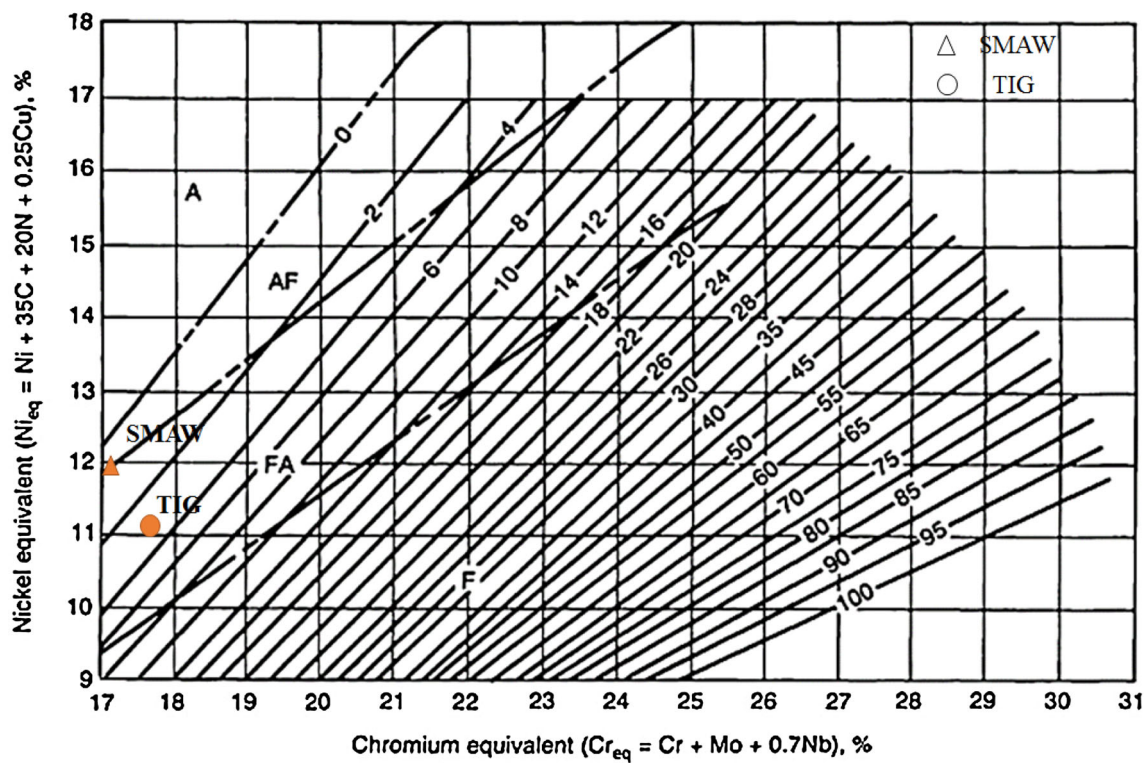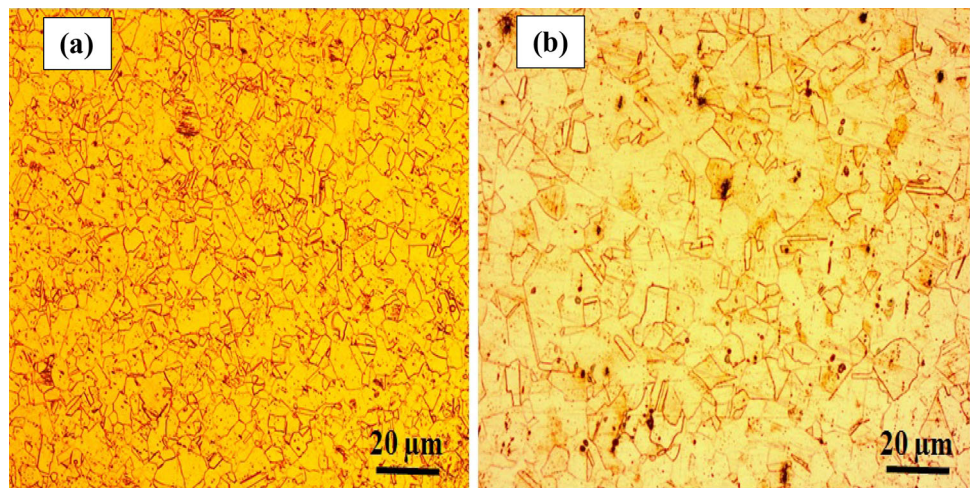

Fig. 3 WRC-1992 diagram showing the position of solidification mode and possibly range of ferrite content in weld samples

Table 3 Chemical composition of the weld metal

Welding process	Chemical composition					WRC-1992		
	Cr	Ni	Mn	Si	C	Cr_{eq}	Ni_{eq}	Cr_{eq}/Ni_{eq}
SMAW	17.04	7.61	3.80	0.48	0.09	17.04	11.96	1.42
TIG	17.80	7.13	3.60	0.50	0.08	17.80	11.13	1.59

EDS is used for determining the chemical composition of the weld metal and is listed in Table 3. It is observed that Cr_{eq} is higher in TIG welding as compared to SMAW, whereas Ni_{eq} was found higher in SMAW welding process. Also, the Cr_{eq}/Ni_{eq} is found to be 1.42 for SMAW and 1.59 for TIG welding. The presence of 0.06 wt.% N is

considered in the bulk of weld metals [24]. According to the WRC-1992 diagram, it can be observed that solidification mode for both the heat input is found to be in ferrite–austenite (FA) mode. The ferrite content was higher in TIG welding (3.5 wt.%) as compared to SMAW (1 wt.%). It is reported that increase in heat input reduces the formation ferrite in the weld metal [20]. Hence, lower heat input results in higher cooling rate. In the present study, lower heat input is found in TIG welding.

Figures 4 and 5 show the microstructure of SMAW and TIG welding. It is observed that the microstructure of SMAW consists of columnar grains in the fusion zone, whereas the microstructure produced by TIG is almost equiaxed. Also, due to more austenite formation in the SMAW and more δ ferrite formation in the TIG, there is a difference in the contrast of the microstructure. As shown in Figs. 4 and 5, the brighter constituent corresponds to the austenitic phase and the darker constituent resembles δ ferrite. In SMAW and TIG welding, the grain growth direction was from grain boundary to weld center. Low magnification of micrograph shows defect-free weld and interphase with weld zone and HAZ. In both the welding techniques, the weld zone consists of δ ferrite and austenite. The δ ferrite was observed in the form of skeletal and lath ferrite, and this is due to restricted diffusion/and or faster cooling rate of alloy in lath ferrite during ferrite–austenite (FA) transformation. Takalo et al. observed that the austenitic solidification majorly depend on the chemical composition of the alloy [21]. The chromium nickel equivalent ratio was calculated according to Eqs 4 and 5 [17].

$$Cr_{eq} = \%Cr + \%\,Mo + 1.5 \times \%Si + 0.5 \times \%Cb + 5 \times \%V + 3 \times \%Al \tag{4}$$

$$Ni_{eq} = \%Ni + 30 \times \%C + 0.87 \times \%Mn + 0.33 \times \%Cu + 30 \times (\%N - 0.045) \tag{5}$$

Psuedo-binary diagram is used for the solidification behavior of the weld pool as shown in Fig. 6. The Cr_{eq}/Ni_{eq} ratio which defines the solidification mode of the weld pool [17].

$$\text{Austenite mode: } L \to (L + \gamma) \to \gamma, \quad (Cr_{eq}/Ni_{eq}) < 1.25 \tag{6}$$

$$\text{Austenite Ferrite mode: } L \to (L + \gamma) \\ \to (L + \gamma + \delta)(\gamma + \delta), \tag{7} \\ 1.25 < (Cr_{eq}/Ni_{eq}) < 1.48$$

$$\text{Ferrite Austenite mode: } L \to (L + \delta) \to (L + \delta + \gamma) \\ \to (\gamma + \delta), \\ 1.48 < (Cr_{eq}/Ni_{eq}) < 1.95 \tag{8}$$

$$\text{Ferrite mode: } L \to (L + \delta) \to \delta \to (\gamma + \delta), \\ (Cr_{eq}/Ni_{eq}) > 1.95 \tag{9}$$

The chromium nickel equivalent ratio was found to be 1.62. Hence, the actual solidification mode is found to be

Fig. 4 Optical and SEM micrograph of SMAW welded Cr–Mn SS
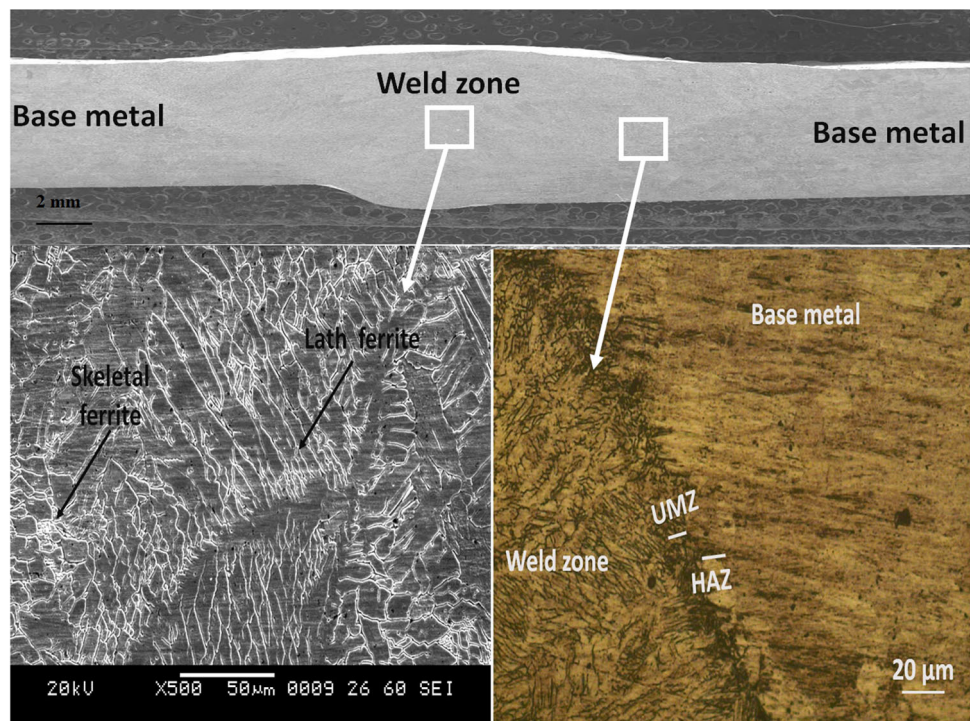
Fig. 5 Optical and SEM micrograph of TIG welded Cr–Mn SS
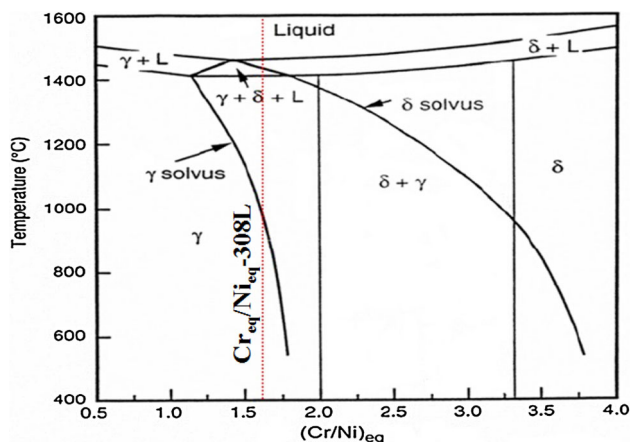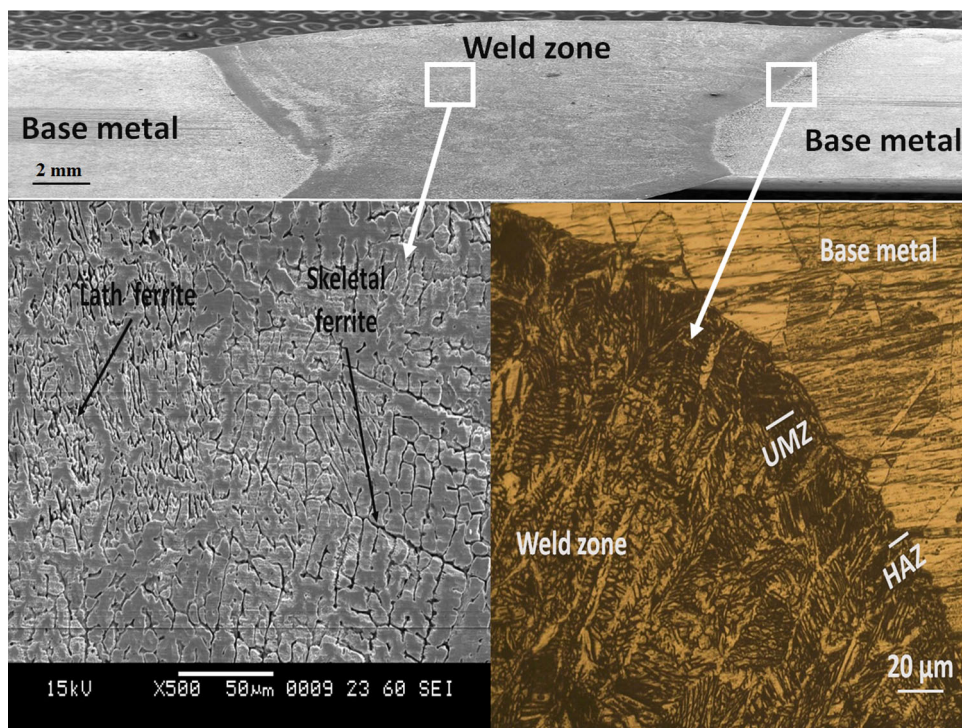

Fig. 6 Psuedo-binary diagram of plotted against (Cr/Ni)$_{eq}$ ratio

FA mode. The results correlate with the predicted solidification mode of WRC-1992 diagram. As the initial solidification starts from ferrite and transforms to austenite, it is interesting to note that peritectic reactions ($L + \delta = \gamma$) cause the formation of austenite. Fu et al. investigated the origin of the lath ferrite in 304 SS during directional solidification and had reported that the formation of austenite is due to peritectic reaction rather than eutectic reactions. Due to the partial eutectic reaction in the weld, partial delta ferrite is retained, and rest of the liquid transforms to austenite directly [22]. The cooling rate of both the weld process defines the formation of δ ferrite in

the weld zone as the solidification mode is ferrite–austenite (FA), and hence, higher cooling rate (low heat input) will result in more δ ferrite in the weld matrix. The formation of skeletal and lath ferrite is also controlled by the cooling rate. When the cooling rate is moderate, it results in more skeletal ferrite, whereas higher cooling rate forms more lathy ferrite in the weld matrix as shown in Figs. 4 and 5. The microstructure of SMAW revealed more skeletal form of ferrite, and TIG welding forms more lath ferrite in the weld zone. The dendrite length and inter-dendritic distance were also calculated for both the welding process and are listed in Table 4. It was found that dendrite length and inter-dendritic distance were smaller for TIG welding as compared to SMAW welding process. Similar results were observed by Subodh and Shahi [18] with varying the heat input. The epitaxial growth/unmixed zone is shown clearly in Figs. 4 and 5 for both the welding process. The width of unmixed zone and HAZ is found to be smaller for TIG welding as compared to SMAW. This is due to lower heat input in TIG welding. Also, grain coarsening of the metal is observed more in SMAW. The ferrite number is also calculated and found higher ferrite number in TIG. The chemical composition of ferrite and austenite phase in the weld zone was calculated from EDS as shown in Fig. 7 and listed in Table 5. It was found that in ferrite matrix the composition of Cr (21.2 wt.%) was higher than in austenite phase (17.1 wt.%). Also, the amount of manganese in the austenite matrix is observed to be higher.

Table 4 Microstructural details of welding

Welding process	Dendrite length (μm)	Inter-dendrite spacing (μm)	Unmixed zone length (μm)	HAZ width (μm)	δ-ferrite by ferritoscope (FN)	
					WM	BM
TIG	31.45	5.72	85.9	79.9	6.7	0.15
SMAW	37.17	13.8	133.8	125.4	3.6	0.15
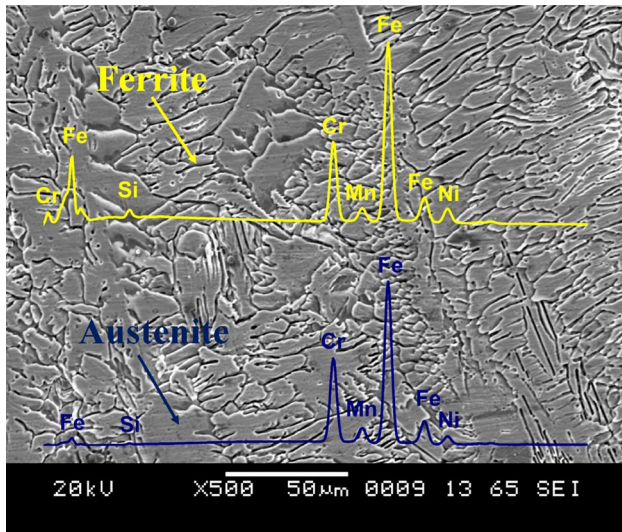
Fig. 7 EDS analysis of ferrite and austenite

Fig. 8 Microhardness of welding

Table 5 Chemical composition of phases (wt.%)

Phase	Chemical composition		
	Cr	Ni	Mn
δ ferrite	21.2	4.7	2.2
Austenite	17.1	6.5	3.4

Mechanical Property

Hardness

Figure 8 compares the hardness values of both the welding process. It is observed that average hardness value of BM was found to be 241 HV (microhardness evaluation of the weld was performed along the transverse direction). It is found that the lower hardness values of weld zone for both the welding process were due to coarse grain cast structure formed during solidification of the welding. The hardness value of TIG is found to be more as compared to SMAW welding process which is mainly due to more δ ferrite in the weld zone of TIG welding [23]. In HAZ region, there is a decrease in hardness of the weld sample in case of SMAW due to grain coarsening. An abrupt increase in the hardness
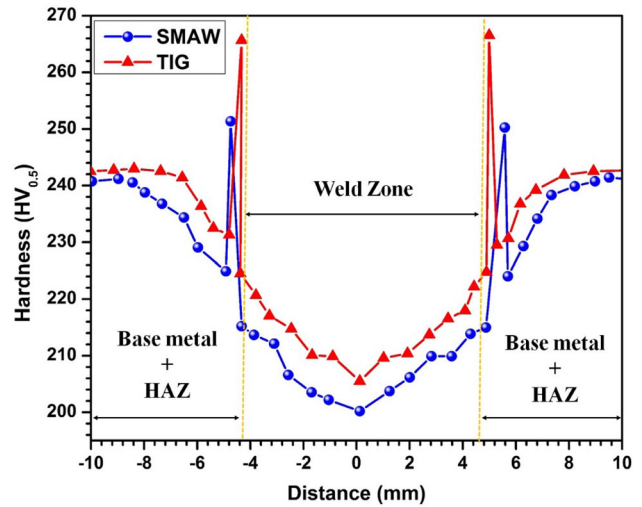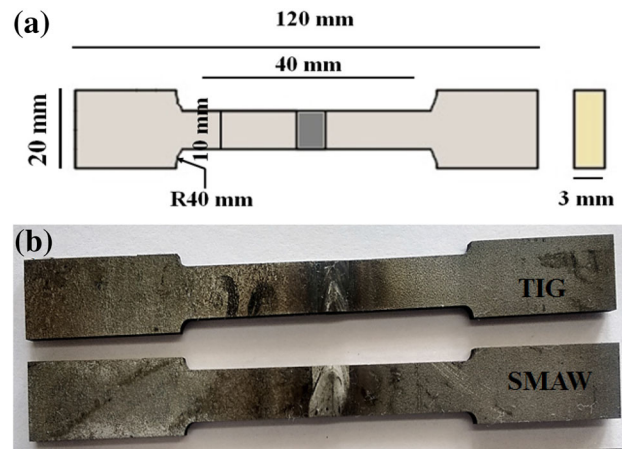

Fig. 9 a Schematic diagram of tensile specimen, b photograph of tensile specimen

in the intermixing of HAZ and the unmixed zone was due to chromium precipitate ($Cr_{23}C_6$) in the weld sample.

Tensile

The schematic representation and photograph image of the tensile specimen are shown in Fig. 9a and b. Three samples

Table 6 Data obtained from tensile test

Welding process	Before strauss			After strauss		
	Ultimate tensile strength (MPa)	% of Elongation	Tensile failure	Ultimate tensile strength (MPa)	% of elongation	Tensile failure
TIG welding	675.86 ± 9[a]	28 ± 1.4	Weld zone	350.56 ± 7	13 ± 1.2	Weld zone
SMAW	610.25 ± 10	32 ± 1.3	Weld zone	320.56 ± 8	15 ± 1.1	Weld zone

[a] Standard deviation
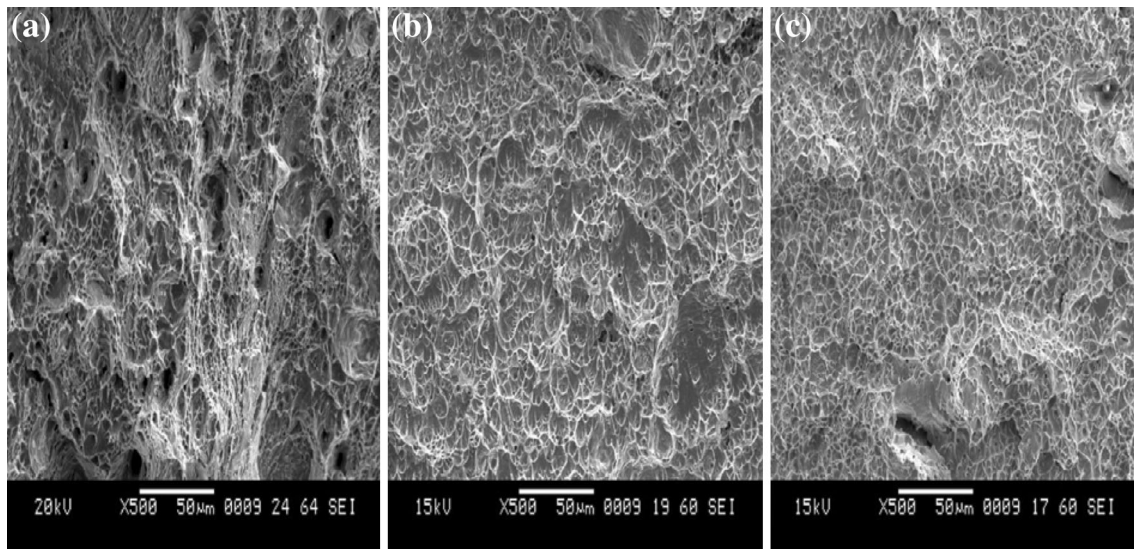
Fig. 10 Fractography of **a** base metal, **b** SMAW and **c** TIG

were prepared for each result, and the average value of the tensile test is shown in Table 6. The tensile strength of BM was found to be 856.01 MPa, whereas, for SMAW and TIG, it was found to be 610.25 and 675.86 MPa, respectively. The increase in ultimate tensile strength of TIG was due to more ferrite in the weld matrix offered better strength to the weld. The results are in agreement with the findings of Korino and Malene [13]. The fractography of the BM, SMAW, and TIG weld are shown in Fig. 10. Base metal shows dimple-like morphology which resembles high degree of ductility. However, for SMAW and TIG weld, the fractography show larger average facet size for SMAW, whereas in case of TIG, little ductility was observed due to fine grains in the weld zone. Figure 11a and b shows fracture surface after modified Strauss test. It was found that ductility of the material gets reduced and grain dropping is observed due to difference in potential in grain and grain boundary. Little facets can be observed in TIG welding due to more ferrite in the weld. Strength of the material also gets reduced after Strauss test for both the weld samples as shown in Table 6.

Corrosion Behavior

Potentiodynamic Polarization Test in 3.5% NaCl Solution (PDP Test)

Figure 12a shows PDP test at 3.5 wt.% NaCl solution. The fitted Tafel slope value of the plots is shown in Table 7. It is observed that the corrosion current density (i_{corr}) of base metal (BM) is higher than weld. The difference in the i_{corr} for BM and weld samples was due to Cr content in the samples. The value of E_{corr} is active for base metal and drifts in the noble direction (positive direction) from SMAW to TIG, respectively. The passive behavior is observed for all the welded samples. Passive potential (i_{pass}) is the potential required to maintain the passivity in the sample. Hence, lower i_{pass} is observed for TIG welding as compared to SMAW welding process. The pitting potential (E_{pit}) is also found to be higher for TIG welding. The resisting potential is calculated for both the welded samples. It is found that resistance potential was higher for TIG welding samples. The high corrosion resistance of TIG is mainly due to high

Fig. 11 Fracture surface after modified Strauss test **a** SMAW, **b** TIG
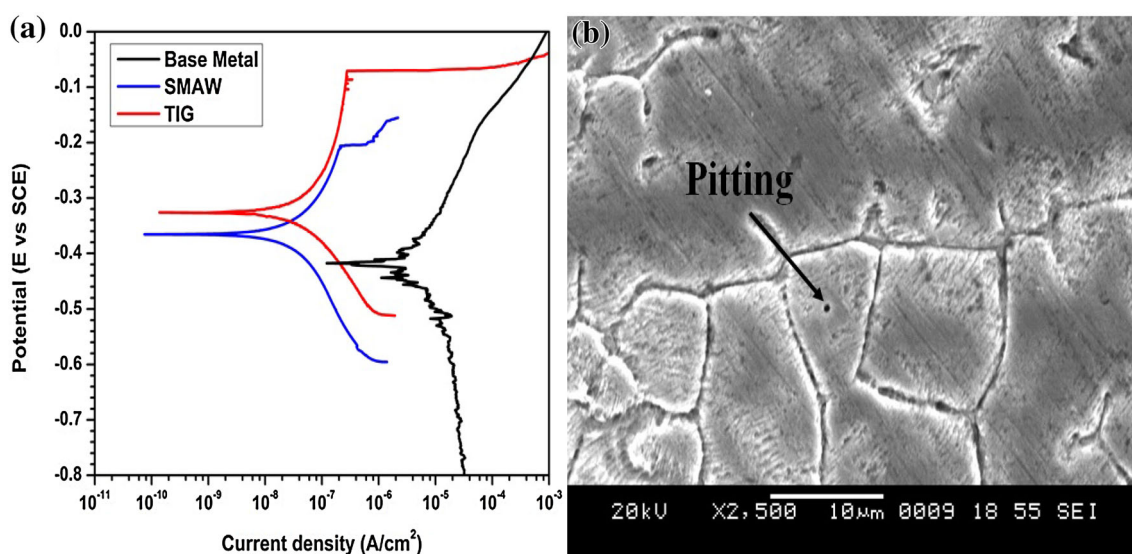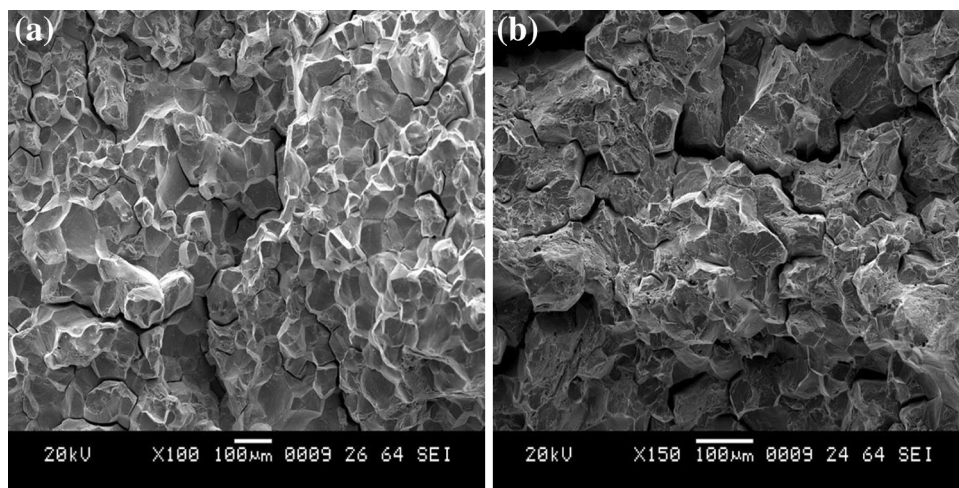

Fig. 12 **a** Potentiodynamic polarization plots of base metal and welding, **b** SEM after PDP test

Table 7 Potentiodynamic polarization data for Cr–Mn ASS at 3.5% NaCl solution

Samples	E_{corr} (mV)	i_{corr} ($\mu A/m^2$)	βa (mV)	βc (mV)	E_{pit} (mV)	$E_{corr} - E_{pit}$ (mV)
BM	−417.3	9.02	330.14	400.47	–	–
SMAW	−336.21	0.204	50.3	56.0	−209.2	127.0
TIG	−327.50	0.015	191.8	146.5	−68.5	259

delta ferrite in the weld [17]. Figure 12b shows the SEM micrograph of samples after PDP test. It is found that maximum pitting was found to be on the austenite phase. Hence, chemical composition of the alloy plays a vital role in corrosion behavior in the weld.

Galvanic Corrosion

Figure 13 shows the galvanic corrosion coupled between base meal and different weld zones (SMAW and TIG).

The base metal shows lower E_{corr} as compared to weld zone of both the process. Thus base metal is more active and is expected to act as the anode and the weld zone as the cathode. From Fig. 13, it is observed that the change in current for all the couple changes with time. The galvanic corrosion for TIG is higher as compared to SMAW. This may be due to more difference in the ferrite and austenite interface. The galvanic corrosion rate was low in the range of $\mu A/cm^2$.
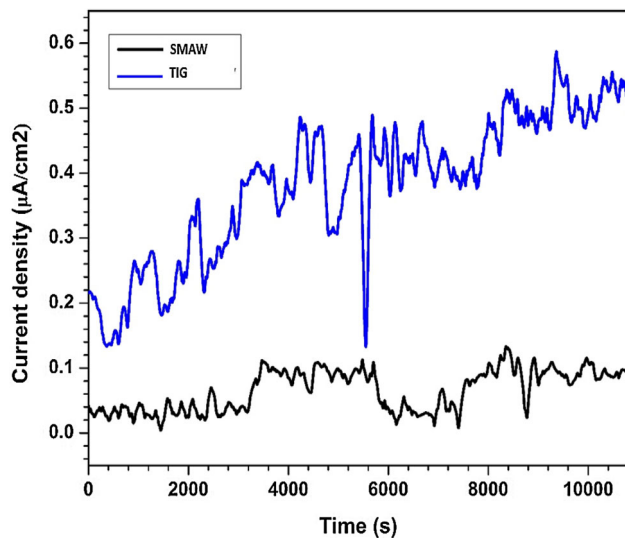
Fig. 13 Time dependence of galvanic corrosion in 3.5% NaCl

Conclusions

1. WRC-1992 diagram is compared with the results of ferritoscope measured values and found that the ferrite content is in good agreement with the results of WRC diagram.

2. Metallurgical inspection of the weld samples shows the formation of skeletal and lath ferrite. SMAW results in higher dendritic length and inter-dendritic distance as compared from TIG welding. Also wider HAZ was observed in SMAW. This may be due to higher heat input in SMAW.

3. Due to more δ ferrite in TIG welding, the value of hardness and tensile strength increases as compared to SMAW. Modified Strauss test shows decrease in tensile strength for both the welding process.

4. Increase in δ ferrite content in TIG welding, the pitting resistance increases as compared to SMAW. Also i_{corr} value is lower in TIG welding. This is due to more Cr content in the weld metal. Also, galvanic current corrosion shows higher current density for TIG than SMAW welding process.

5. Both the welding process using 308L electrode can be used for joining Cr–Mn SS. However, welding with TIG welding is recommended due to its better mechanical and corrosion behavior as compared with SMAW.

References

1. F.A. Garner, H.R. Brager, D.S. Gelles, J.M. McCarthy, Neutron irradiation of Fe–Mn, Fe–Cr–Mn and Fe–Cr–Ni alloys and an explanation of their differences in swelling behavior. J. Nucl. Mater. **148**, 294–301 (1987)

2. R.V. Taiwade, S.J. Patre, A.P. Patil, Studies on welding and sensitization of chrome-manganese austenitic stainless steel. Trans. Indian Inst. Metals **64**, 513–518 (2011)

3. M. Coetzee, P.G.H. Pistorius, The welding of experimental low-nickel Cr–Mn–N stainless steels containing copper. J. S. Afr. Inst. Min. Metall. **96**, 99–108 (1996)

4. M.L.G. Byrnes, M. Grujicic, W.S. Owen, Nitrogen strengthening of a stable austenitic stainless steel. Acta Metall. **35**, 1853–1862 (1987)

5. E. Werner, Solid solution and grain size hardening of nitrogen-alloyed austenitic steels. Mater. Sci. Eng. A **101**, 93–98 (1988)

6. K.H. Tseng, C.Y. Hsu, Performance of activate TIG process in austenitic stainless steel welds. J. Mater. Process. Technol. **211**, 503–512 (2011)

7. T. Mohandas, G.M. Reddy, M. Naveed, A comparative evaluation of gas tungsten and shielded metal arc welds of a ferritic stainless steel. J. Mater. Process. Technol. **94**, 133–140 (1999)

8. A.R. Galvis, W. Hormaza, Characterization of failure modes for different welding processes of AISI/SAE 304 stainless steels. Eng. Fail. Anal. **18**, 1791–1799 (2011)

9. P. Yayla, E. Kaluc, K. Ural, Effects of welding processes on the mechanical properties of HY 80 steel weldments. Mater. Des. **28**, 1898–1906 (2007)

10. P. Bala Srinivasan, V. Muthupandi, W. Dietzel, V. Sivan, An assessment of impact strength and corrosion behaviour of shielded metal arc welded dissimilar weldments between UNS 31803 and IS 2062 steels. Mater. Des. **27**, 182–191 (2006)

11. D.J. Kotecki, T.A. Siewert, WRC-1992 constitution diagram for stainless steel weld metals: a modification of the WRC-1988 diagram. Weld. J. **71**, 171–178 (1992)

12. Y. Cui, C.D. Lundin, Austenite-preferential corrosion attack in 316 austenitic stainless steel weld metals. Mater. Des. **28**, 324–328 (2007)

13. P.S. Korinko, S.H. Malene, Considerations for the weldability of types 304L and 316L stainless steel. Pract. Fail. Anal. **4**, 61–68 (2001)

14. J. Yan, M. Gao, X. Zeng, Study on microstructure and mechanical properties of 304 stainless steel joints by TIG, laser and laser-TIG hybrid welding. Opt. Lasers Eng. **48**, 512–517 (2010)

15. V. Muthupandi, P. Bala Srinivasan, S.K. Seshadri, S. Sundaresan, Effect of weld metal chemistry and heat input on the structure and properties of duplex stainless steel welds. Mater. Sci. Eng A **358**, 9–16 (2003)

16. Y. Weng (ed.), *Ultrafine grained steels* (Springer, Beijing, 2009)

17. R. Mohammed, G.M. Reddy, K.S. Rao, Microstructure and pitting corrosion of shielded metal arc welded high nitrogen stainless steel. Def. Technol. **11**, 237–243 (2015)

18. S. Kumar, A.S. Shahi, Effect of heat input on the microstructure and mechanical properties of gas tungsten arc welded AISI 304 stainless steel joints. Mater. Des. **32**, 3617–3623 (2011)

19. M. Dadfar, M.H. Fathi, F. Karimzadeh, M.R. Dadfar, A. Saatchi, Effect of TIG welding on corrosion behavior of 316L stainless steel. Mater. Lett. **61**, 2343–2346 (2007)

20. J. Verma, R.V. Taiwade, R.K. Khatirkar, S.G. Sapate, A.D. Gaikwad, Microstructure, mechanical and intergranular corrosion

behavior of dissimilar DSS 2205 and ASS 316L shielded metal arc welds. Trans. Indian Inst. Metals **70**, 225–237 (2017)

21. N. Suutala, T. Takalo, T Moisio.: The relationship between solidification and microstructure in austenitic and austenitic–ferritic stainless steel welds. Metall. Trans. A. **10**, 512–514 (1979)

22. J.W. Fu, Y.S. Yang, Origin of the lathy ferrite in AISI 304 stainless steel during directional solidification. J. Alloys Compd. **580**, 191–194 (2013)

23. R. Mohammed, G. Madhusudhan Reddy, K.S. Rao, Effect of filler wire composition on microstructure and pitting corrosion of nickel free high nitrogen stainless steel GTA welds. Trans. Indian Inst. Metals **69**, 1919–1927 (2016)

24. Steve Lampman, *Weld Integrity and Performance: A Source Book Adapted* (ASM International, Materials Park, 1997), p. 250